

# The HH34 outflow as seen in [Fe II]1.64 $\mu$ m by LBT-LUCI<sup>\*</sup> (Research Note)

S. Antonucci<sup>1</sup>, A. La Camera<sup>2</sup>, B. Nisini<sup>1</sup>, T. Giannini<sup>1</sup>, D. Lorenzetti<sup>1</sup>, D. Paris<sup>1</sup>, and E. Sani<sup>3</sup>

<sup>1</sup> INAF - Osservatorio Astronomico di Roma, Via di Frascati 33, 00040 Monte Porzio Catone, Italy

<sup>2</sup> DIBRIS, Università di Genova, Via Dodecaneso 35, 16146, Genova, Italy

<sup>3</sup> INAF-Osservatorio Astrofisico di Arcetri, Largo Enrico Fermi 5, 50125 Firenze, Italy

Received ; accepted

## ABSTRACT

**Context.** Dense atomic jets from young stars copiously emit in [Fe II] IR lines, which can, therefore, be used to trace the immediate environments of embedded protostars.

**Aims.** We want to investigate the morphology of the bright [Fe II] 1.64 $\mu$ m line in the jet of the source HH34 IRS and compare it with the most commonly used optical tracer [S II].

**Methods.** We analyse a 1.64 $\mu$ m narrow-band filter image obtained with the Large Binocular Telescope (LBT) LUCI instrument, which covers the HH34 jet and counterjet. A Point Spread Function (PSF) deconvolution algorithm was applied to enhance spatial resolution and make the IR image directly comparable to a [S II] HST image of the same source.

**Results.** The [Fe II] emission is detected from both the jet, the (weak) counter-jet, and from the HH34-S and HH34-N bow shocks. The deconvolved image allows us to resolve jet knots close to about 1'' from the central source. The morphology of the [Fe II] emission is remarkably similar to that of the [S II] emission, and the relative positions of [Fe II] and [S II] peaks are shifted according to proper motion measurements, which were previously derived from HST images. An analysis of the [Fe II]/[S II] emission ratio shows that Fe gas abundance is much lower than the solar value with up to 90% of Fe depletion in the inner jet knots. This confirms previous findings on dusty jets, where shocks are not efficient enough to remove refractory species from grains.

**Key words.** Stars: protostars, Stars: mass-loss, Stars: jets, ISM: jets and outflows, ISM: abundances, Techniques: image processing

## 1. Introduction

The Herbig-Haro (HH) object HH34 and its related jet represent one of the most remarkable and well studied flow of matter from a young star. The HH34 object is composed by a couple of large bow-shocks (HH34 S and HH34 N) that are symmetrically displaced at a distance of about 0.2 pc with respect to the embedded driving source HH34 IRS. Associated with the two bow-shocks, a highly collimated chain of knots originating from HH34 IRS forms a bright optical jet that points towards the HH34 S bow (Bührke et al. 1988)

Imaging observations of a larger field around HH34 have revealed a number of additional bow shocks at larger distances, indicating that the total extent of this bipolar flow is almost 3 pc (Eisloffel & Mundt 1997; Devine et al. 1997). The driving source HH34 IRS is a  $\sim 0.5 M_{\odot}$  actively accreting protostar with  $L_{\text{bol}} \sim 15 L_{\odot}$  (Antonucci et al. 2008).

The HH34 flow has been the subject of intense observational campaigns that include spectro-photometry and kinematical measurements at both optical and IR wavelengths (e.g., Heathcote & Reipurth 1992; Eisloffel & Mundt 1992; Morse et al. 1992, 1993; Reipurth et al. 2002; Beck et al. 2007). Detailed proper motion studies were conducted with multi-epoch HST images, which were used to model the time-history of the flow (Raga & Noriega-Crespo 1998; Raga et al. 2012). These studies

show that the HH 34 jet is subject to variations in velocity and jet axis direction, which might be due to precession of the outflow induced by a possible companion.

Several IR spectroscopic investigations have been performed on the HH34 jet, showing that it copiously emits in both [Fe II] and H<sub>2</sub> transitions (Podio et al. 2006, Takami et al. 2006, Garcia Lopez et al. 2008, Davis et al. 2011). The IR spectroscopy has revealed for the first time the presence of a counter-jet (Garcia Lopez et al. 2008), which has later been imaged with Spitzer (Raga et al. 2011). The aim of this note is to complement the previous near-IR spectroscopic investigations of HH34 with high quality imaging in [Fe II]1.64 $\mu$ m, as obtained with the instrument LUCI (Seifert et al. 2003) mounted on the Large Binocular Telescope (LBT). We compare the morphology of the jet in the IR with that of a commonly used optical tracer like [S II]. The [Fe II] 1.64 $\mu$ m line traces dense ( $\sim 10^4 \text{ cm}^{-3}$ ) shocked gas at low excitation ( $T_{\text{ex}} = 11\,000 \text{ K}$ ): being in the infrared, it can reveal details on the more embedded jet regions that remain obscured at optical wavelengths.

Previous imaging observations in [Fe II] of HH34 were performed by Stapelfeldt et al. (1991) and Reipurth et al. (2000); this latter observation was obtained with the HST-NICMOS camera. The sensitivity of these images was, however, not high enough to study the details of the IR jet and identify the embedded counter-jet. Sensitive spectro-imaging in [Fe II] were obtained by Davis et al. (2011), but they cover only a small 3'' $\times$ 3'' field around the HH34 IRS source.

In the present note, we describe the [Fe II] morphology of the flow in comparison with an optical [S II] image taken with

Send offprint requests to: Simone Antonucci, e-mail: simone.antonucci@oa-roma.astro.it

\* Based on observations obtained with the Large Binocular Telescope.

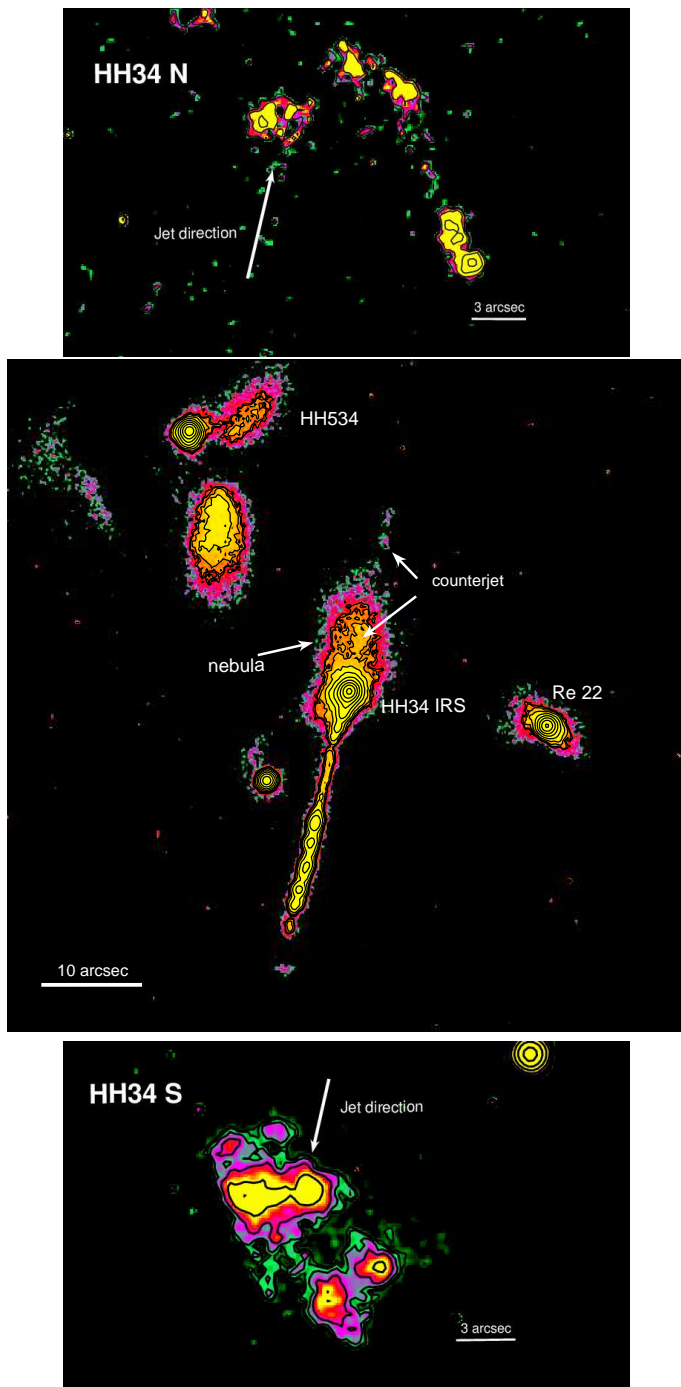


**Fig. 1.** LBT-LUCI image of the HH34 region obtained with a narrow-band filter centred on the [Fe II] 1.64 $\mu$ m transition. The middle panel shows the region that comprises the HH34 collimated jet and its driving source, HH34 IRS. The top and bottom panels display the region around the two large bow shocks HH34 N and HH34 S, respectively, which are located at about 100'' from HH34 IRS. Background areas display a mean rms of  $9 \times 10^{-19}$  erg s $^{-1}$  cm $^{-2}$  pixel $^{-1}$ . The bottom contour mark the 5  $\sigma$  level in the upper and lower panels and the 10  $\sigma$  level in the central panel. The remaining nine contours are traced using a logarithmic scale with the highest level corresponding to a flux 100 times greater than the first contour. We note that in spite of the large nebulosity associated with the source, the HH34 counter-jet is detected as a faint collimated emission.

the HST. Such a comparison has been improved by the application of a suitable deconvolution method (La Camera et al. 2014) to the seeing limited LBT image. In addition, we measure the [Fe II]/[S II] ratio along the jet and relate it to iron depletion variations in the different shock episodes.

## 2. Observations and reduction

Imaging with LUCI ( $4' \times 4'$  field of view with a pixel scale of  $0''.118/\text{pix}$ ), which was equipped with the [Fe II] filter ( $\lambda_{\text{eff}} = 1.646\mu\text{m}$ ,  $\Delta\lambda = 0.018\mu\text{m}$ ), was carried out at the LBT on two different nights (Feb 19 and Apr 1 2013) using a dithering technique for a total combined exposure time of 30 minutes. The reduction of the two datasets was achieved using the LBT pipeline developed at the Rome Observatory, in which the raw frames are first pre-reduced by subtracting a median stack dark image and by applying a flat-field that is obtained by combining a set of sky flats (each subtracted by its own dark and normalised by its own median background level). After this step, cosmetic masks are created to flag out saturated regions, cosmic rays events, and bad pixels; maps of background are then subtracted from each image. Finally, for each scientific frame, an accurate astrometric calibration is computed to correct for geometrical distortions; this allows the use of SWarp (Bertin et al. 2002) to both resample the processed images and create the final mosaic stack. Given that the seeing conditions were similar during the two nights of observations, the final [Fe II] image was obtained from the combination of the two exposures. The Point Spread Function (PSF) full-width-at-half-maximum of this final image, which was measured on several field stars, is about  $0''.85$ .

## 3. Results and analysis

### 3.1. Large-scale morphology

The central portion of the final image covering an area of  $75'' \times 75''$  around HH 34 is shown in the middle panel of Fig. 1. The collimated southern jet (detected in optical images and composed by blue-shifted gas) emerges from the IR bright HH34 IRS source and is clearly visible. The northern counter-jet is also detected, although at a much fainter level. The region around HH34 IRS is characterised by a large nebulosity, which prevents a clear view of the red-shifted counter-jet close to the central source. An enhanced collimated emission is, however, observed along the direction of the jet axis, which indicates that the counter-jet extends close to the source, as already shown spectroscopically by Garcia-Lopez et al. (2008). The emission knots observed in the counter-jet are about an order of magnitude fainter than the corresponding blue-shifted jet knots. Assuming this is due to the extinction, this implies an  $A_V$  of about 12-13 mag towards the brightest counter-jet knots (at a distance of  $\sim 15''$  from source). The extinction value in the jet blue-shifted and symmetrically displaced knots, as estimated through IR spectroscopy of [Fe II] line ratios, is about 1.5 mag (Podio et al. 2006). To account for the different extinctions, a  $\text{H}_2$  column density that is about a factor of ten higher in the counter jet than in the blue-shifted jet is therefore needed. Such a higher column density in the red-shifted region is not supported by millimeter maps of the region (Johnstone & Bally, 2006). On the other hand, the HH34 jet and counter-jet appear symmetric in the Spitzer IRAC images, which are sensitive to  $\text{H}_2$  emission (Raga et al. 2011). It is possible that the counter-jet has a different excitation structure with the molecular component that is more enhanced with respect to the atomic one.

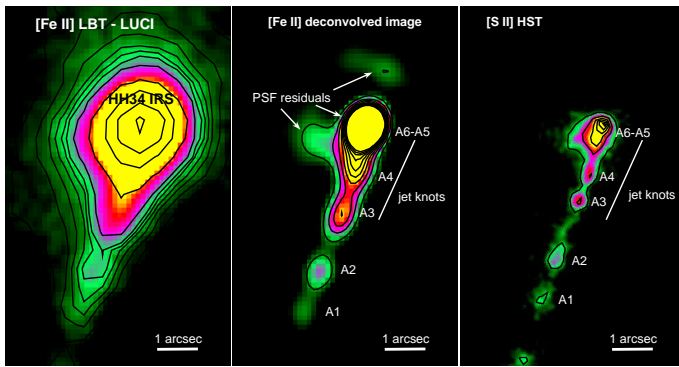


**Fig. 2.** [Fe II]1.64 $\mu\text{m}$  image of the central HH34 IRS region. The left and middle panels show the original image and the image deconvolved by adopting the algorithm described in La Camera et al. (2014), respectively. In the left panel, a HST image in [S II] at 6716+6730  $\text{\AA}$  taken in 2007 is shown from comparison (Hartigan et al. 2011).

In addition to the HH34 jet, the 1.64 $\mu\text{m}$  image shows extended nebulosities that originate from the IR sources IRS5 and Re22, but no collimated emission that is indicative of shock-excited gas is associated with the HH534 object (Reipurth et al. 2002).

Symmetrically displaced at about 100'' from the source, we detected both the HH 34 N and HH34 S bow shocks (top and bottom panels of Fig. 1, respectively). They do not present structures that are morphologically different from those observed in [S II] with HST. Figure 1 shows that the HH34 N bow shock appears to not be aligned with the direction of the jet. This is consistent with the variations of the jet axis due to precession already observed in optical HST images.

### 3.2. Image deconvolution and small scale morphology

As we see from Fig. 1, the close surrounding of HH34 IRS is dominated by continuum emission from the bright source and its reflection nebula. To reduce the contribution of the continuum emission and get information on the jet structure at resolutions comparable with HST images, we have applied a deconvolution algorithm optimised for separating point-like structures from a diffuse extended continuum to the image, which is named *multi-component Richardson-Lucy* (MC-RL) (La Camera et al. 2014). The MC-RL method is based on the decomposition of the target as a sum of a point source (the star) and an extended source (the jet). By assuming Poisson noise, a regularisation term is added to the negative logarithm of the likelihood, which enforces smoothness of the jet component. A Richardson-Lucy like method is finally employed for the minimisation of the obtained function through iterations alternating between the two components.

The deconvolution algorithm was applied to the central region of the image, which covers the entire HH34 collimated jet, by using 500 iterations. The PSF for the deconvolution was extracted from the average of three (point-like) stars present in the image field by means of the Software Package AIRY (Correia et al., 2002; La Camera et al., 2012).

Figure 2 shows the inner part of the HH34 jet before and after the deconvolution. The PSF of the deconvolved image is around 0''.24. For comparison, the figure also shows the most recent (2007) HST image in [S II] at 6730 $\text{\AA}$  (Hartigan et al. 2011). In the HST image the HH34 IRS continuum from the nebula is weak, and the jet is traced close to the source through sev-

eral emission knots, which have been named after Reipurth et al. (2000) from A1 to A7, for decreasing distance from the source. In the [Fe II] deconvolved image, we are able to resolve knots from A1 to A5, which are located at about 1'' from the central source. The position of the [Fe II] knot peaks are shifted with respect to the knots in the [S II] image due to the proper motion of the jet. Raga et al. (2012) have recently studied the kinematics of the HH34 jet using HST images with a nine-year time baseline. They found that the jet knots follow a ballistic motion and the tangential velocity of the internal A knots is about 200  $\text{km s}^{-1}$ . Assuming a distance of 414 pc (Menten et al. 2007), we expect the knots to have moved by about 0''.5 during the time-line between the [S II] and [Fe II] observations. In A1, A2, and A3, we measure a shift between 0''.4-0''.5, which is consistent with previous proper motion results. This evidence implies in turn that there is no large difference in the [Fe II] and [S II] morphologies, at least at a half-arcsec resolution.

Figure 3 shows the [Fe II] deconvolved image of the entire collimated jet compared to the [S II] image. Given the small number of field stars available for realignment, we estimate that the two images are registered with an accuracy of about 0''.2. The jet morphology in the two tracers is again very similar. In the figure, the main knot peaks detected in [Fe II] are indicated with crosses and also reported on the [S II] image for comparison. All the knots visible in [S II] are also detected in [Fe II] with no appreciable variations in morphology but with the expected shifts in position due to proper motion. These shifts range between 0''.4 and 0''.7 in the C-L knots with no apparent trends with distance. Raga et al. (2012) derived that the tangential velocity decreases from about 200  $\text{km s}^{-1}$  to about 170  $\text{km s}^{-1}$  going from the internal A knots to the more external C-E knots. We do not detect variations in the angular shifts corresponding to this velocity decrease, which would correspond to about 0''.1. This is, however, lower than the estimated image alignment accuracy.

### 3.3. [Fe II]/[S II] ratio and Fe abundance

The LUCI narrow-band image has been flux calibrated by considering the 2MASS *K*-band magnitude of four stars that are detected in the field. Zero point magnitude variations of the order of 0.3 mag have been measured among the selected stars, which results in a 20% uncertainty on the absolute flux calibration of the image. Considering that the effective wavelengths of the Fe narrow-band and 2MASS *K*-band filters (1.646 $\mu\text{m}$  and 1.662 $\mu\text{m}$ , respectively) differ by less than 0.02 $\mu\text{m}$  and that the stars used for determining the zero point do not present peculiar spectral shapes in the near-IR range, we expect that the error related to the different bandwidths of the filters is negligible with respect to the local fluctuations of the sky background. Table 1 reports the [Fe II] fluxes measured on individual knots, by considering an aperture with a radius of 0''.6 (representing the typical size of the brightest knots) and centred on the knot peak (coordinates are given in the Table).

The [S II] HST image has also been flux-calibrated to compare the [Fe II]/[S II] line ratios. With this aim, we used the star 2MASS J05353040-0627072, which is the only optically bright and isolated star present in the field. For this star, we adopted an *R*-band magnitude of 17.95 $\pm$ 0.15 from the average of the *R* photometry from the GSC 2.3.2 (Lasker et al., 2008) and USNO-B1.0 (Monet et al., 2003) catalogues (18.1 and 17.8 mag, respectively). The relative uncertainty on flux calibration is therefore 15%.

The [Fe II] 1.64 $\mu\text{m}$  transition has a critical density of the order of 10<sup>4</sup>  $\text{cm}^{-3}$  and an excitation temperature of  $\sim$ 11 000  $\text{cm}^{-1}$ .

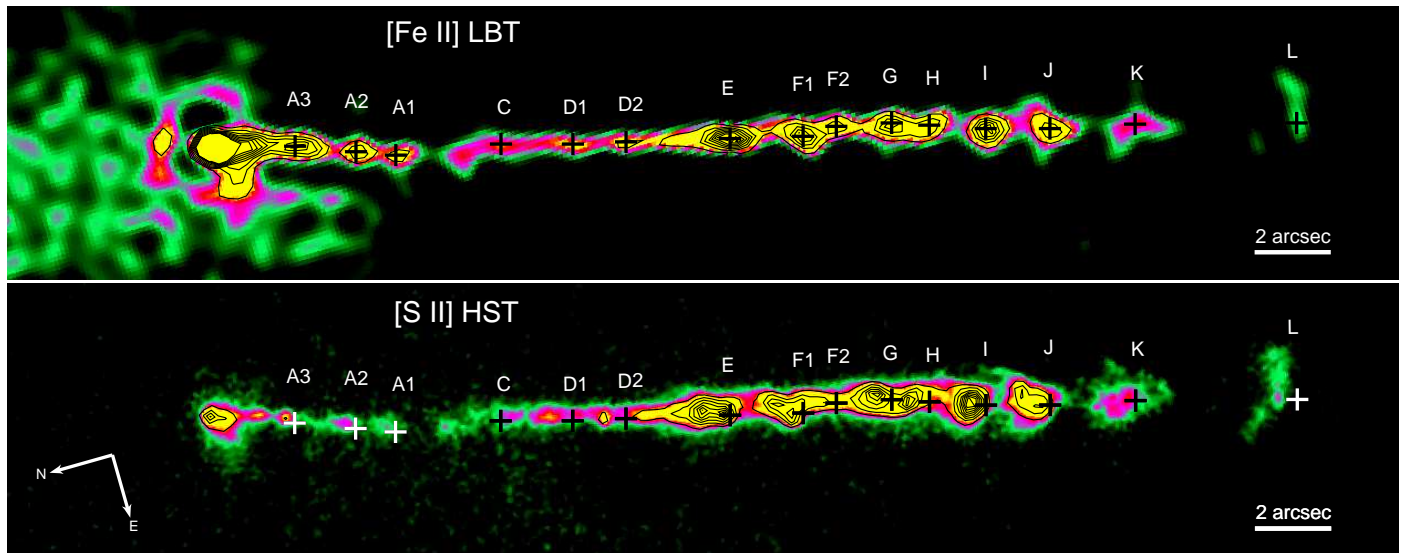


**Fig. 3.** [Fe II]1.64 $\mu\text{m}$  deconvolved image of the entire HH34 jet is shown in comparison with the HST image in [S II] at 6716+6730 Å. Both images are rotated for a better comparison. Crosses mark the peaks of the emission knots detected in the [Fe II] image. The same positions are reported on the [S II] image to make evident the shifts due to the jet proper motion.

In comparison, [S II] (6716+6730 Å) lines have critical densities of the order of  $10^3 \text{ cm}^{-3}$  and excitation temperatures of the order of  $20000 \text{ cm}^{-1}$ . Therefore, [Fe II] is more sensitive than [S II] to dense gas at low excitation. Nisini et al. (2005) compared the relative intensity profiles of [Fe II] and [S II] lines expected in the post-shocked gas, showing that the emission zone of the [Fe II]1.64 $\mu\text{m}$  line overlaps with that of the [S II] optical lines, although it is broader and covers a larger area in the post-shocked region. However, these spatial differences are well below the resolution of our observations, being the cooling zone of the post-shocked gas only about  $10^{14} \text{ cm}$  wide (i.e.  $0''.02$  at 414 pc) (Hartigan et al. 1994).

Given the above considerations, the [Fe II]1.64 $\mu\text{m}$ /[S II] (6716+6730 Å) line ratio is sensitive to the shock physical conditions, in particular for temperatures up to 20000 K and in the density range between  $10^3$  and  $10^5 \text{ cm}^{-3}$  (see Fig. 4). This ratio is, however, also sensitive to the relative Fe/S abundance in the shocked gas. Iron, being a refractory element, is depleted on grains in the dusty interstellar medium. If jets are dusty, shocks can erode the grains and release Fe in gaseous form in a percentage that depends on the shock strength and pre-shock density (e.g., Draine 2003). Several studies have shown that the abundance of Fe gas along jets is indeed much lower than solar with percentages of depletion that considerably change among shocks and range from  $\sim 10\%$  up to  $90\%$  (i.e. Nisini et al. 2002, 2005, Podio et al. 2006, Giannini et al. 2008, 2013). In particular, Podio et al. (2006) derived that the abundance of Fe gas along the HH34 jet, which is measured using the ratio of [Fe II]1.64 $\mu\text{m}$ /[P II]1.18 $\mu\text{m}$  lines, is only about 10% of the solar value. In Fig. 4, we compare the [Fe II]1.64 $\mu\text{m}$ /[S II] (6716+6730 Å) ratio in the various knots along the jet with the predicted values by assuming solar Fe/S abundance ratio. Abundance values were taken from Asplund et al. (2006). For this comparison, we have measured the [S II] intensity in the knots by considering the peak shifts with respect to the positions given in Table 1 due to the proper motion. Observed values have also been corrected for extinction by assuming the  $A_V$  values estimated by Podio et al. (2006), which are namely  $A_V=7$  mag in the A knots and  $A_V=1.5$  mag in the more external C-L knots (see also Garcia

**Table 1.** [Fe II] 1.64 $\mu\text{m}$  line fluxes.

knot	R.A. (J2000)			DEC (J2000)			$F^a$ ( $10^{-15} \text{ erg s}^{-1} \text{ cm}^{-2}$ )
	h	m	s	°	'	''	
A3	5:35:29.89			-6:27:00.6			6.1
A2	5:35:29.92			-6:27:02.0			2.7
A1	5:35:29.95			-6:27:03.2			1.5
C	5:35:29.99			-6:27:05.8			1.3
D1	5:35:30.02			-6:27:07.5			1.3
D2	5:35:30.04			-6:27:09.0			1.4
E	5:35:30.09			-6:27:11.6			8.8
F	5:35:30.11			-6:27:13.5			5.9
G	5:35:30.14			-6:27:15.7			5.0
H	5:35:30.16			-6:27:16.8			3.8
I	5:35:30.19			-6:27:18.3			5.7
J	5:35:30.22			-6:27:19.9			3.4
K	5:35:30.26			-6:27:22.1			1.3
L	5:35:30.3			-6:27:26.3			0.4

<sup>a</sup>Fluxes measured in a  $0''.6$  radius beam centred at the given coordinates. Flux calibration uncertainty is of the order of 20%.

Lopez et al. 2008). An error of about 1 mag can be considered for these visual extinction estimates: this is basically due to the uncertainty on the rate coefficients of the [Fe II] lines used for the  $A_V$  determination (see, e.g., Giannini et al. 2008). The figure shows that the observed ratios are always significantly lower than the predicted values, irrespective of the assumed physical conditions. This agrees with Fe being largely depleted from gas phase. We point out that the presented comparison assumes that [Fe II] and [S II] come from the same spatial region. However, as discussed above, [Fe II] covers a larger post-shocked region with respect to [S II], so the observed values should be corrected for their relative filling factors before comparison. This correction would make the observed ratios even lower, thus exacerbating the difference with models that assume solar values.

From the ratios of several optical/IR forbidden lines, Podio et al. (2006) and Garcia Lopez et al. (2008) determined that the density in the HH34 jet varies from  $\sim 10^4$  to  $\sim 1-3 \cdot 10^3 \text{ cm}^{-3}$  in the inner A and outer C-L knots, respectively, with a temperature in the range 6000-14000 K. Assuming these conditions, from

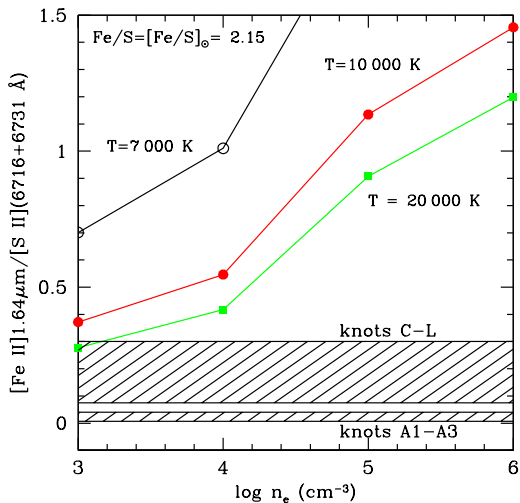


**Fig. 4.** [Fe II]1.64 $\mu\text{m}$ /[S II](6716+6731 $\text{\AA}$ ) intensity ratio, as predicted by NLTE statistical equilibrium calculations, as a function of the electron density and for temperatures of 10 000 K and 20 000 K. Solar abundances from Asplund et al. (2006) are assumed. The dashed areas indicate the range of extinction corrected values measured in the internal knots A and the external knots from C to L. The reported ranges also include the uncertainties from both image calibrations and extinction. The measured ratios are always below the predicted value, irrespective to the assumed temperature and density, which indicates a Fe abundance lower than solar.

Fig. 4 we infer that the Fe gas phase abundance is  $\sim 1\text{-}10\%$   $\text{Fe}_{\odot}$  for knot A and  $\sim 15\text{-}90\%$   $\text{Fe}_{\odot}$  for knots C-L. These results show evidence that a larger Fe depletion is found in the inner knots with respect to the rest of the jet. This dependence of Fe depletion on the distance from the driving source was also observed in the HH1 jet (Nisini et al. 2005). Other refractory species, like Ca, show the same trend of decreasing gas-phase abundance in the inner jet regions (Podio et al. 2009). These trends might be due to a higher density or lower shock velocity in the inner regions, which would diminish the efficiency of dust disruption.

*Acknowledgements.* We kindly thank Pat Hartigan for providing the [S II] HST image.

We acknowledge the support from the LBT-Italian Coordination Facility for the execution of observations, data distribution and reduction.

The LBT is an international collaboration among institutes in the United States, Italy, and Germany. LBT corporation partners are: the University of Arizona on behalf of the Arizona university system; the Istituto Nazionale di Astrofisica, Italy; the LBT Beteiligungsgesellschaft, Germany, representing the Max-Planck Society, the Astrophysical Institute of Potsdam, and Heidelberg University; The Ohio State University, and the Research Corporation, on behalf of the University of Notre Dame, University of Minnesota, and University of Virginia.

The Guide Star Catalogue-II is a joint project of the Space Telescope Science Institute and the Osservatorio Astronomico di Torino.

The USNO-B1.0 catalog was created by Dave Monet and collaborators at <http://www.nofs.navy.mil/data/fchpix/>

## References

- Antonucci, S., Nisini, B., Giannini, T., & Lorenzetti, D. 2008, A&A, 479, 503  
 Asplund, M., Grevesse, N., & Jacques Sauval, A. 2006, Nuclear Physics A, 777, 1  
 Beck, T. L., Riera, A., Raga, A. C., & Reipurth, B. 2007, AJ, 133, 1221  
 Bertin, E., Mellier, Y., Radovich, M., Missonnier, G., Didelon, & P., Morin, B., 2002, ASPC, 281, 228

- Bührke, T., Mundt, R., & Ray, T. P. 1988, A&A, 200, 99  
 Correia, S., Carillet, M., Boccacci, P., Bertero, M., & Fini, L. 2002, A&A, 387, 733  
 Davis, C. J., Cervantes, B., Nisini, B., et al. 2011, A&A, 528, A3  
 Devine, D., Bally, J., Reipurth, B., & Heathcote, S. 1997, AJ, 114, 2095  
 Draine, B. T. 2003, ARA&A, 41, 241  
 Eisloffel, J., & Mundt, R. 1992, A&A, 263, 292  
 Eisloffel, J., & Mundt, R. 1997, AJ, 114, 280  
 Garcia Lopez, R., Nisini, B., Giannini, T., et al. 2008, A&A, 487, 1019  
 Giannini, T., Calzoletti, L., Nisini, B., et al. 2008, A&A, 481, 123  
 Giannini, T., Nisini, B., Antonucci, S., et al. 2013, ApJ, 778, 71  
 Johnstone, D., & Bally, J. 2006, ApJ, 653, 383  
 Hartigan, P., Frank, A., Foster, J. M., et al. 2011, ApJ, 736, 29  
 Hartigan, P., Morse, J. A., & Raymond, J. 1994, ApJ, 436, 125  
 Heathcote, S., & Reipurth, B. 1992, AJ, 104, 2193  
 La Camera, A., Carillet, M., Olivieri, C., Boccacci, P., & Bertero, M. 2012, Proc. SPIE, 84453E  
 La Camera, A., Antonucci, S., Bertero, M., et al. 2014, PASP, 126, 180  
 Lasker, B. M., Lattanzi, M. G., McLean, B. J., et al. 2008, AJ, 136, 735  
 Menten, K. M., Reid, M. J., Forbrich, J., & Brunthaler, A. 2007, A&A, 474, 515  
 Monet, D., G., Levine, S., E., Canzian, B., Ables, H., D., Bird, A., R., et al., 2003, AJ, 125 984.  
 Morse, J. A., Hartigan, P., Cecil, G., Raymond, J. C., & Heathcote, S. 1992, ApJ, 399, 231  
 Morse, J. A., Heathcote, S., Hartigan, P., & Cecil, G. 1993, AJ, 106, 1139  
 Nisini, B., Caratti o Garatti, A., Giannini, T., & Lorenzetti, D. 2002, A&A, 393, 1035  
 Nisini, B., Bacciotti, F., Giannini, T., et al. 2005, A&A, 441, 159  
 Raga, A., & Noriega-Crespo, A. 1998, AJ, 116, 2943  
 Takami, M., Chrysostomou, A., Ray, T. P., et al. 2006, ApJ, 641, 357  
 Podio, L., Bacciotti, F., Nisini, B., et al. 2006, A&A, 456, 189  
 Podio, L., Medves, S., Bacciotti, F., Eisloffel, J., & Ray, T. 2009, A&A, 506, 779  
 Raga, A. C., Noriega-Crespo, A., Rodríguez-González, A., et al. 2012, ApJ, 748, 103  
 Raga, A. C., Noriega-Crespo, A., Lora, V., Stapelfeldt, K. R., & Carey, S. J. 2011, ApJ, 730, L17  
 Reipurth, B., Yu, K. C., Heathcote, S., Bally, J., & Rodríguez, L. F. 2000, AJ, 120, 1449  
 Reipurth, B., Heathcote, S., Morse, J., Hartigan, P., & Bally, J. 2002, AJ, 123, 362  
 Seifert, W., Appenzeller, I., Baumeister, H., Bizenberger, P., Bomans, D., et al. 2003, Proc. SPIE, 4841, 962  
 Stapelfeldt, K. R., Scoville, N. Z., Beichman, C. A., Hester, J. J., & Gautier, T. N., III 1991, ApJ, 371, 226